J Neurooncol (2012) 110:315–323
DOI 10.1007/s11060-012-0974-5

LABORATORY INVESTIGATION

Growth properties of SF188/V+ human glioma in rats in vivo observed by magnetic resonance imaging

Rachel Grossman · Betty Tyler · Henry Brem · Charles G. Eberhart · Silun Wang · De-Xue Fu · Zhibo Wen · Jinyuan Zhou

Received: 10 February 2012 / Accepted: 12 September 2012 / Published online: 27 September 2012

Abstract SF188/V+ is a highly vascular human glioma model that is based on transfection of vascular endothelial growth factor (VEGF) cDNA into SF188/V− cells. This study aims to assess its growth and vascularity properties in vivo in a rat model. Thirty-two adult rats were inoculated with SF188/V+ tumor cells, and, for comparison, five were inoculated with SF188/V− tumor cells. Several conventional magnetic resonance imaging (MRI) sequences were acquired, and several quantitative structural (T_2 and T_1), functional [isotropic apparent diffusion coefficient (ADC) and blood flow], and molecular [protein and peptide-based amide proton transfer (APT)] MRI parameters were mapped on a 4.7 T animal scanner. In rats inoculated with SF188/V+ tumor cells, conventional T_2-weighted images showed a highly heterogeneous tumor mass, and post-contrast T_1-weighted images showed a heterogeneous, strong enhancement of the mass. There were moderate increases in T_2, T_1, and ADC, and large increases in blood flow and APT in the tumor, compared to contralateral brain tissue. Microscopic examination revealed prominent vascularity and hemorrhage in the VEGF-secreting xenografts as compared to controls, and immunohistochemical staining confirmed increased expression of VEGF in tumor xenografts. Our results indicate that the SF188/V+ glioma model exhibits some MRI and histopathology features that closely resemble human glioblastoma.

Keywords SF188/V+ · Brain tumor · Glioma · Angiogenesis · APT imaging · MRI

Electronic supplementary material The online version of this article (doi:10.1007/s11060-012-0974-5) contains supplementary material, which is available to authorized users.

R. Grossman · B. Tyler · H. Brem
Department of Neurosurgery, Johns Hopkins University School of Medicine, Baltimore, MD, USA

C. G. Eberhart
Department of Pathology, Johns Hopkins University School of Medicine, Baltimore, MD, USA

S. Wang · Z. Wen · J. Zhou (✉)
Division of MR Research, Department of Radiology, Johns Hopkins University School of Medicine, 600 N. Wolfe Street, Park 336, Baltimore, MD 21287, USA
e-mail: jzhou@mri.jhu.edu

D.-X. Fu
Department of Oncology, Johns Hopkins University School of Medicine, Baltimore, MD, USA

J. Zhou
F.M. Kirby Research Center for Functional Brain Imaging, Kennedy Krieger Institute, Baltimore, MD, USA

Introduction

Glioblastoma (GBM) is the most common primary brain tumor in adults and accounts for more than 50 % of all gliomas. It is also the most deadly of the gliomas, with a median survival of 12–14 months [1]. Few patients are alive 5 years after diagnosis [2, 3], even with maximal therapy, consisting of tumor resection, intensity-modulated radiation therapy (RT), temozolomide (TMZ), and the locally delivered 1,3-bis(2-chloroethyl)-1-nitrosourea (BCNU) wafers (Gliadel) [4]. GBM is a highly vascularized tumor, notorious for irregular blood vessels, extensive vascular proliferation, and increased expression of angiogenic factors, most notably the vascular endothelial growth factor (VEGF). The high expression of VEGF on tumor endothelium, correlated with tumor hypoxia [5], results in growth and proliferation of

endothelial cells, areas of necrosis, and overall poor prognosis [6].

Recognizing the critical need for new approaches to improve the outcome for patients with GBM has resulted in numerous pre-clinical studies. However, evaluation of new therapeutic strategies requires an accurate animal model, which mirrors as closely as possible the imaging, pathological, and clinical features of the human disease. Rodent glioma models are commonly used in the neuro-oncology field [7, 8]. However, the majority of these models lack important pathological features when compared to human GBM [9, 10]. SF188/V+ is a human glioma model that is based on transfection of VEGF cDNA into SF188/V− cells [11] in order to produce an angiogenic cell line that expresses a high amount of VEGF. This vascular cell line has been used in pharmacokinetic (PK) studies to test the combination of cytotoxic and anti-angiogenesis compounds [12, 13].

During the last 3 decades, magnetic resonance imaging (MRI) became a standard modality for neuroimaging. The most common MRI sequences used in the clinic include T_2-weighted, fluid-attenuated inversion recovery, and gadolinium-enhanced T_1-weighted images, which are used to determine the extent of tumor involvement and to assess tumor response to therapy [14–16]. In addition, there are several advanced imaging techniques, such as diffusion imaging to probe tumor cellularity [17–20], perfusion and blood volume imaging to detect the microvascular integrity [21, 22], and proton MR spectroscopic imaging to determine metabolic status [23, 24]. Recently, a specific chemical exchange-based saturation transfer MRI technique [25], dubbed amide proton transfer (APT) imaging [26], was proposed, which can be used to detect over-expressed, endogenous mobile proteins and peptides (micromolar–millimolar range) in tumor [27–30].

The SF188/V+ glioma model could potentially play an important role in angiogenesis research in the neuro-oncology field. To our knowledge, however, the MRI characteristics of SF188/V+ tumor xenografts in vivo have not been reported until now. In this study, we characterize in vivo the growth and vascularity properties of the SF188/V+ human glioma cell line in a rodent model using a multi-parameter MRI protocol, including conventional (structural), functional, and molecular MRI sequences.

Materials and methods

Cell lines

The SF188/V+ and SF188/V− human glioma cell lines were kindly provided by Dr. Gallo (Temple University, Philadelphia, PA, USA; currently Mount Sinai School of Medicine, New York, NY, USA). The parental SF188/V− cell line was originally provided by the Brain Tumor Research Center, University of California, San Francisco, CA, USA. As described by Ma et al. [11], mouse full-length VEGF164 cDNA (583 bp) was originally constructed in the Bluescript KS vector (Strategene) within *Bam*HI and *Eco*RI sites of the vector. It was cloned into the PcDNA3 mammalian expression vector by standard methods. The VEGF sense plasmids contained the coding sequences for the sense VEGF164 under the transcription control of the CMV promoter. The sense VEGF164 cDNA was then transfected into SF188 cells (SF188/V+). Colonies were selected by G418 at a concentration of 800 mg/ml.

Prior to implantation, the SF188/V+ and SF188/V− human glioma cell lines were grown in DMEM with Earle salts and L-glutamine (Mediatech), supplemented with 10 % fetal bovine serum (Gemini Bioproducts), 2 mmol/l sodium pyruvate (Mediatech), 0.1 mmol/l DMEM-nonessential amino acids (Mediatech), and gentamycin (Mediatech). The cells were grown at 37 °C in a humidified incubator with 5 % CO_2.

Tumor cell implantation

The study was approved by the Johns Hopkins Animal Care and Use Committee (ACUC), and all procedures were conducted in compliance with their regulations. Thirty-seven male, athymic rats (Harlan Bioproducts, Indianapolis, IN, USA) weighing 200–250 g were anesthetized by intraperitoneal injection of 3–5 ml/kg body weight of a stock solution, containing ketamine hydrochloride 25 mg/ml, xylazine 2.5 mg/ml, and 14.25 % ethyl alcohol in 0.9 % NaCl. Anesthetized animals were secured in a stereotactic apparatus. The scalp was cleaned, and a midline incision was made to expose the skull. A burr hole was drilled by an automatic drill, centered 3 mm to the left of the sagittal suture, avoiding the sagittal sinus, and 5 mm posterior to the coronal suture. A 25-µl Hamilton syringe with a 26-gauge needle attached to the stereotactic frame was used to inject either 1.5, 3, or 5 million SF188/V+ cells ($n = 14$, 9, or 9, respectively) or 1.5 million SF188/V− cells ($n = 5$) in 5 µl sterile saline at a depth of 5 mm from the skull. The needle was then withdrawn, and the skin was closed with sutures. The rats were returned to their cages and received a regular rat diet and water ad libitum. The rats were monitored daily for weight loss and neurological deficit.

Animal care during MRI

On each of the experimental days indicated, animals implanted with tumor cells were re-anesthetized with 5 % isoflurane in a mixture of 75 % air and 25 % O_2 in a plexiglass container for about 5 min for induction, followed by breathing of 1.5–2.5 % isoflurane through a nose

cone fixed with an MRI coil setup during MRI procedures. While anesthetized, a PE-10 catheter was placed into the dorsal tail vein to administer gadolinium contrast agents prior to MRI. The rat head and body were fixed and taped to the coil and cradle to avoid motion artifacts. Throughout the MRI procedure, rats were constantly monitored online through a small-animal respiratory-gating system connected with optic fibers, and the breathing rate of the animal was kept at 40 ± 5 breaths per minute by adjusting the isoflurane ratio (1.5–2.5 %) in the breathing mixture.

MRI experiments

MRI data were acquired using a horizontal bore 4.7 T animal MR imager (Bruker Biospin) with an actively decoupled cross-coil setup (a 70-mm body coil for radiofrequency transmission and a 25-mm surface coil for signal reception). Local shimming was performed on the brain.

First, T_2-weighted images (fast spin-echo or FSE acquisition; repetition time or TR = 3 s; echo time or TE = 64 ms; five slices; slice thickness = 1.5 mm; number of averages or NA = 2) were acquired in both the horizontal plane (matrix = 256 × 192; field of view or FOV = 42 × 32 mm^2) and the coronal plane (matrix = 192 × 192; FOV = 32 × 32 mm^2). Then, several quantitative MRI parameters were acquired, including T_2 (TR = 3 s; TE = 30, 40, 50, 60, 70, 80, and 90 ms; NA = 4), T_1 (inversion recovery; predelay = 3 s; TE = 30 ms; inversion recovery time = 0.05, 0.3, 0.6, 1.2, 1.8, 2.5, and 3.5 s; NA = 4), isotropic apparent diffusion coefficient (ADC; TR = 3 s; TE = 80 ms; *b*-values = 0, 166.7, 333.3, 500, 666.7, 833.3, and 1,000 s/mm^2; NA = 8), blood flow (arterial spin labeling or ASL [31], 3-s labeling at a distance of 20 mm away from the imaging slice; TR = 6 s; TE = 28.6 ms), and APT (frequency-labeling offsets of ±3.5 ppm; TR = 10 s; TE = 30 ms; saturation power = 1.3 μT; saturation time = 4 s; NA = 16). As described previously [27, 28], these maps were obtained with single-shot, spin-echo, echo-planar imaging (EPI) data acquisition (matrix = 64 × 64; FOV = 32 × 32 mm^2; single-slice; slice thickness = 1.5 mm). The image slice was overlapped with one of the T_2-weighted images. Finally, T_1-weighted images (TR = 700 ms; TE = 10 ms; NA = 10) with and without gadolinium enhancement were acquired with the same geometry and location as the T_2-weighted images. About 90 min were used to run all these experiments.

Data analysis

All data processing was performed using Interactive Data Language (IDL, Research Systems, Boulder, CO, USA). Data processing methods and procedures used were the same as our previous publications [27, 28]. Briefly, The T_1 map, T_2 map, and ADC map were fitted, using the following equations: $I = A + B \exp(-TI/T_1)$, $I = I_0 \exp(-TE/T_2)$, and $I = I_0 \exp(-b\ ADC)$, respectively. The CBF map was reconstructed from images with and without labeling using previously described methods [31]. As described previously [27, 28], the APT signal was calculated using the MTR asymmetry (MTR_{asym}) at the offset of 3.5 ppm with respect to water: $MTR_{asym}(3.5\ ppm) = S_{sat}(-3.5\ ppm)/S_0 - S_{sat}(+3.5\ ppm)/S_0$, where S_{sat} and S_0 are the signal intensities with and without selective radiofrequency irradiation, respectively.

For the quantitative image analysis, we used the signal abnormalities on the high-resolution T_2-weighted images and gadolinium-enhanced T_1-weighted images, as well as APT images as a basis for defining regions of interest (ROIs). For all cases, the tumor ROIs covered most areas of the lesions with the signal abnormalities on MRI. For each rat, the same tumor region was analyzed for all MRI variables. Ventricles and peritumoral edema were excluded. We have previously demonstrated that novel APT imaging can separate the tumor from peritumoral edema and cerebrospinal fluid (hyperintensity vs. isointensity) [27–29]. The MRI parameter difference between ipsilateral and contralateral to the tumor side for all MRI measures was analyzed with a paired, two-tailed *t* test. The level of significance was set at $P < 0.05$.

Histology

When rats were deeply anesthetized (breathing stopped), the animals were perfused with 75 ml sterile saline followed by 75 ml 4 % paraformaldehyde. After euthanasia, brains were excised and preserved in 4 % paraformaldehyde at 4 °C for a week for proper tissue fixation. When the brains were sectioned, the acquired MR images and intrinsic landmarks, such as the corpus callosum and the ventricles, were used for reference. Next, 10-μm-thick cryostat sections were cut and processed for hematoxylin and eosin (H&E) staining for histopathological evaluation by a board-certified neuropathologist. Immunohistochemical analysis was performed using standard techniques with rabbit anti-VEGF (1:1,200, SC-152; Santa Cruz Biotechnology, Santa Cruz, CA, USA).

Results

Radiographic features of tumor xenografts

Rats that were each inoculated with either 1.5, 3, or 5 million SF188/V+ cells ($n = 9$ for each group) grew a tumor mass during the first 3 weeks post-implantation. These tumor masses became clearly visible (~1 mm) in

MRI between 1 and 3 weeks after tumor inoculation, and then continued to grow. After the tumors formed, their morphological features became very similar, independent of the tumor cell number inoculated. In a second set of experiments comparing xenograft formation using cells with high or low levels of VEGF, the SF188/V− tumors grew at a slower rate than the SF188/V+ xenografts ($n = 5$ for each group), which is consistent with a previous study [11].

Figure 1 shows one example of the longitudinal changes of SF188/V+ tumor xenografts in rats on the T_2-weighted MR images from 1 to 7 weeks post-implantation (5 million tumor cells implanted). In the initial 2 weeks post-implantation, a tiny T_2-hypointense lesion was observed at the injection site. Then, a T_2-hyperintense tumor mass started to form at 3 weeks post-implantation and grew rapidly from 3 to 5 weeks. Starting at 5 weeks post-implantation, the tumor became extremely heterogeneous on the T_2-weighted images, possibly due to the acute or chronic hemorrhage [32]. The mass effect was apparent, as reflected by the displacement of the central structure. Hydrocephalus was also clearly observed. These effects became more exaggerated at the last MRI time point (7 weeks post-tumor inoculation), where the tumor occupied a large part of the left hemisphere.

Figure 2 shows another example of the MR images of SF188/V+ tumor xenografts in the rat brain at 2 weeks post-implantation (3 million tumor cells implanted). This SF188/V+ tumor grew very fast. T_2-weighted images showed a large lesion at 2 weeks post-implantation. The lesion was extremely heterogeneous, due to the acute or chronic hemorrhage. On the T_1-weighted images (without contrast agents injected), the tumor was also very heterogeneous, with scattered punctate hyperintense foci, which indicated the hemosiderin deposition from the subacute

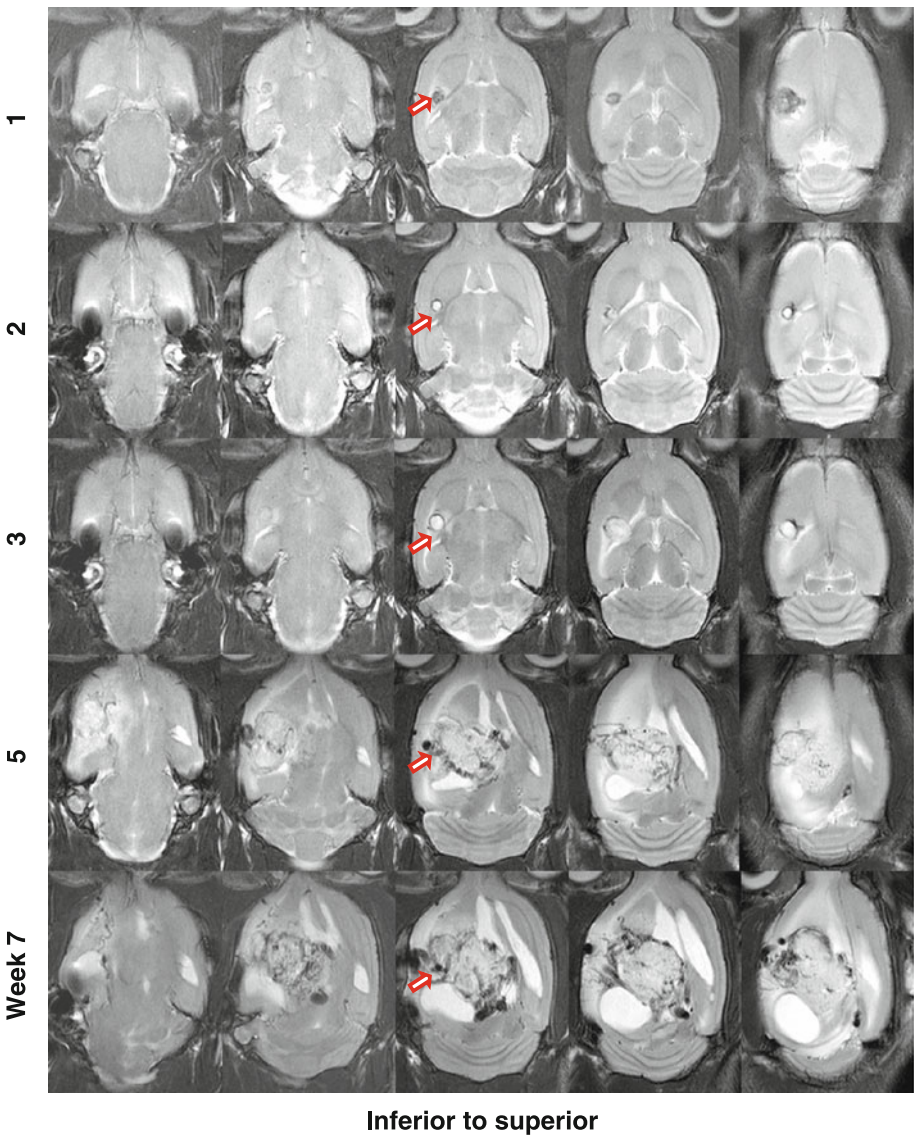

Fig. 1 T_2-weighted MR images in the axial plane of SF188/V+ human glioma xenografts in a rat at different time points post-implantation (5 million cells implanted). The tumor shows heterogeneity on the T_2-weighted MR images as time progresses

hemorrhage. The gadolinium-enhanced T_1-weighted images showed large heterogeneous enhancement in the tumor.

Quantitative results of tumor xenografts

Multi-parameter MR maps measured for an SF188/V+ tumor at 2 weeks post-implantation (3 million tumor cells implanted; the same rat as Fig. 2) and an SF188/V− tumor at 2 weeks post-implantation (1.5 million tumor cells implanted) are shown in Fig. 3a, b, respectively. Unlike SF188/V+, the SF188/V− tumor demonstrates low or even no gadolinium enhancement on the post-contrast T_1-weighted images. In the SF188/V+ tumor model, as expected, T_2, T_1, ADC, blood flow, and APT were all hyperintense in the tumor region, compared to the contralateral brain tissue. The SF188/V+ tumor shows much higher blood flow and APT-MRI signals that likely reflect hemorrhagic changes as compared to the SF188/V− tumor. Note that the heterogeneity of the tumor, observed on the T_2-weighted and T_1-weighted images, was slightly averaged on these low-resolution quantitative MR maps due to the partial volume effect.

The comparison of these quantitative MRI parameters for SF188/V+ tumors (2–4 weeks post-implantation; $n = 14$) and the contralateral hemispheres is given in Table 1. There were significantly higher MRI parameters (T_2, T_1, ADC, blood flow, and APT) in the tumor area than in the contralateral brain tissue ($P < 0.01$ for blood flow; $P < 0.001$ for the others). There were particularly high blood flow (1,247 ml/100 g/min) and APT (11.0 % of the bulk water intensity) signals in the SF188/V+ tumor, compared to the contralateral brain tissue (117 ml/100 g/min and −1.8 %, respectively), as well as to other tumor models, such as 9L (85.3 ml/100 g/min [33] and 2.7 % [28]) and U87MG (61.3 ml/100 g/min and 3.1 % [28]). The high blood flow in the SF188/V+ tumor xenografts suggests intratumoral vascular changes such as neovascularization. The notable APT hyperintensity in SF188/V+ may be due to a much higher concentration of mobile proteins and peptides, such as cytosolic proteins and secreted proteins (serum albumin).

Histology

Microscopic examination of H&E-stained brain sections revealed changes consistent with the imaging characteristics (Fig. 4). In xenografts generated from cells expressing either high (SF188/V+) or low (SF188/V−) levels of VEGF in which animals were sacrificed after 2 weeks, vascular dilatation and associated hemorrhage were prominent in the lesions expressing the angiogenesis factor. Interestingly, dilatation and hemorrhage were noted in vascular elements in the host brain adjacent to tumor xenografts, suggesting the

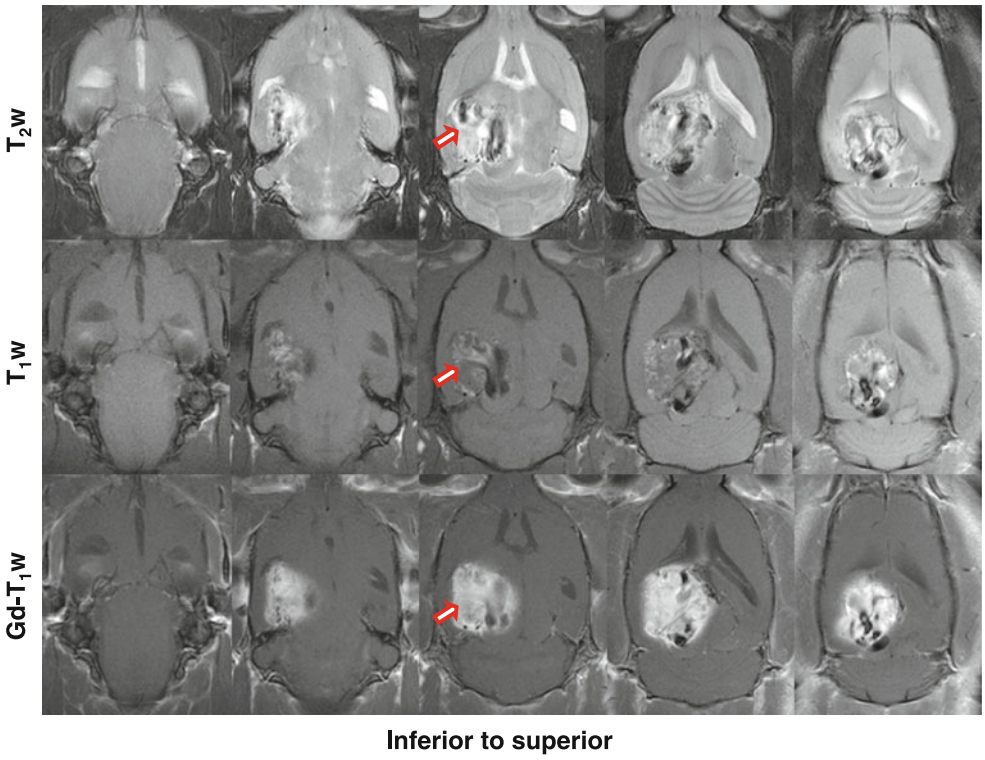

Fig. 2 T_2-weighted, T_1-weighted, and gadolinium-enhanced T_1-weighted MR images in the axial plane of SF188/V+ human glioma xenografts in a rat at 2 weeks post-implantation (3 million cells implanted). Both T_2-weighted and T_1-weighted images show a heterogeneous mass with areas of high and low signals. Post-contrast T_1-weighted MR images show a large enhancement

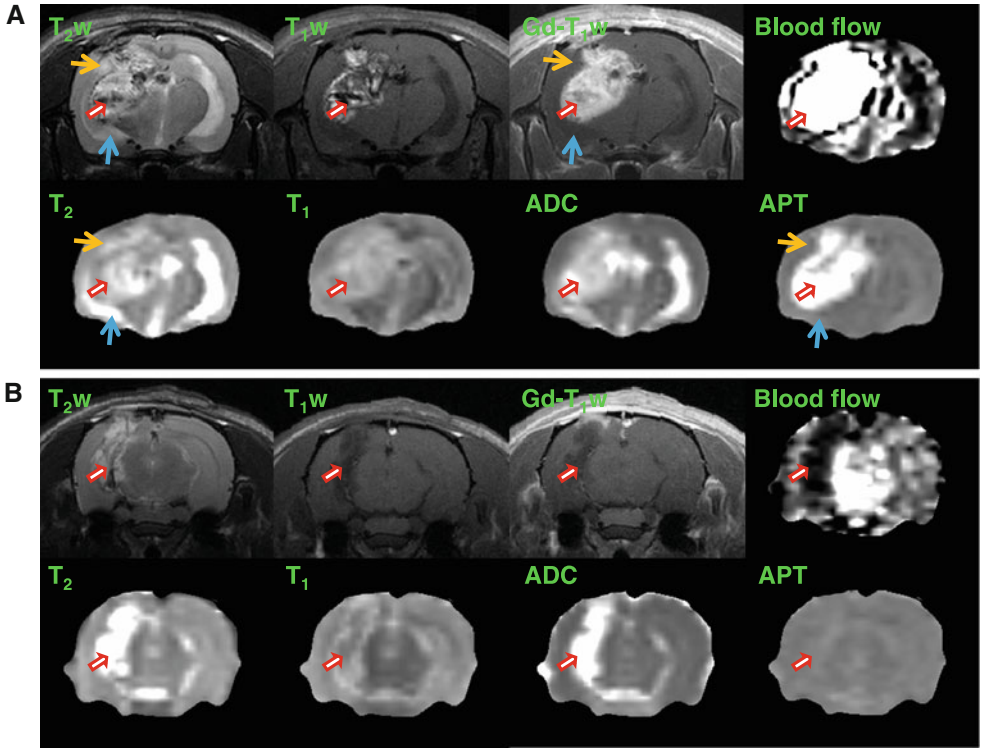

Fig. 3 T_2-weighted, T_1-weighted, and gadolinium-enhanced T_1-weighted MR images and the corresponding quantitative MR maps in the coronal plane. **a** SF188/V+ human glioma xenografts in a rat at 2 weeks post-implantation (3 million cells implanted). **b** SF188/V− human glioma xenografts in another rat at 2 weeks post-implantation (1.5 million cells implanted). All images for each rat were acquired for the same position. The display windows were: T_2 (0–100 ms), T_1 (0.5–2 s), ADC (0–2 × 10^{-9} m^2/s), blood flow (0–200 ml/100 g/min), and APT (−20 to 20 % of the bulk water signal intensity). *Red arrows* tumor mass, *orange arrows* peritumoral edema, *blue arrows* cerebrospinal fluid. Unlike SF188/V+, the SF188/V− tumor demonstrates invisible gadolinium enhancement. The SF188/V+ tumor shows much higher blood flow (4,799 ml/100 g/min vs. 25 ml/100 g/min) and APT-MRI (23.6 vs. 0.2 %) signals than the SF188/V− tumor

Table 1 MRI parameters (value ± SE) measured for the SF188/V+ brain tumor model in rats (2–4 weeks post-implantation; $n = 14$)

	T_2 (ms)	T_1 (s)	ADC (10^{-9} m^2/s)	Blood flow (ml/100 g/min)	APT (% water intensity)
Contralateral	55.4 ± 0.8***	1.35 ± 0.03***	0.83 ± 0.01***	117 ± 24**	−1.8 ± 0.2***
Tumor	69.9 ± 2.4***	1.76 ± 0.04***	1.46 ± 0.03***	1247 ± 316**	11.0 ± 1.3***

Statistical difference between the ipsilateral and contralateral hemispheres: ** $P < 0.01$; *** $P < 0.001$

VEGF secreted by the tumor could diffuse and affect blood vessel biology at some distance from the main neoplastic mass. In contrast, almost no large, dilated vessels were noted in the SF188/V− xenograft.

Intracranial SF188/V+ tumors removed after 4 weeks of growth were larger but had similar vascular changes. The cellular tumor xenografts contained numerous mitotic figures and apoptotic bodies as well as scattered blood vessels, many of which were extremely dilated. Some intravascular thrombosis was noted, along with extravascular hemorrhage. In some xenografts, a network of smaller vessels was also prominent, and some tightly packed tumor nodules had emerged. To confirm the increased expression of VEGF in SF188/V+ cells growing in vivo, we stained xenografts for VEGF using standard immunohistochemical techniques. Moderate to high VEGF staining was noted in and around vessels of SF188/V+ cells, while only weak staining was noted in the SF188/V− xenograft.

Discussion

The understanding that angiogenesis is crucial to tumor growth and progression has led to numerous pre-clinical studies [34] and clinical trials [35] testing the efficacy of anti-angiogenic therapy in the last 2 decades. These pre-

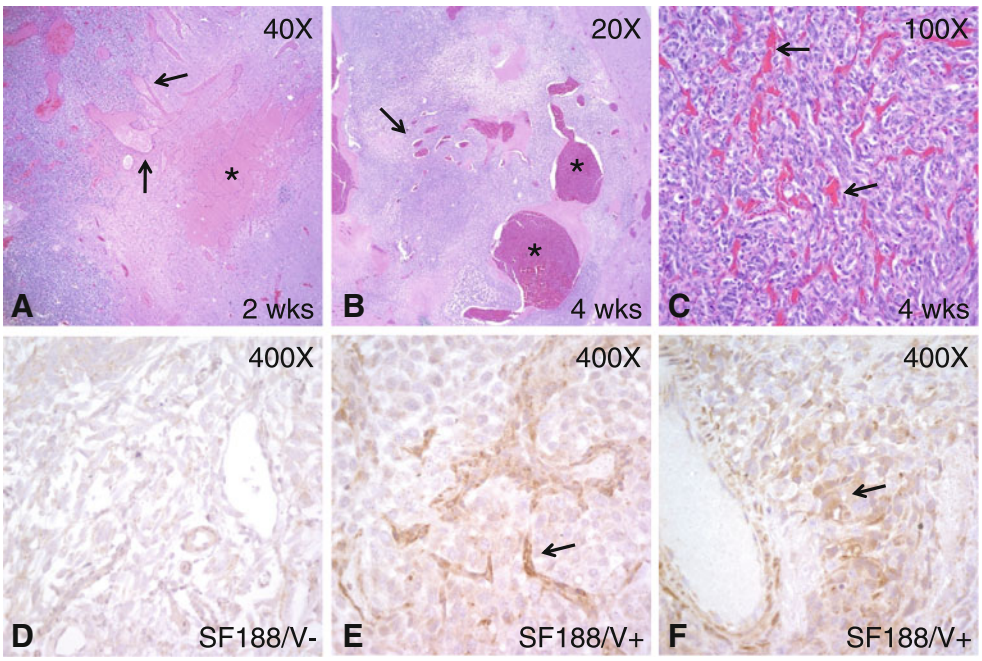

Fig. 4 Microscopic and immunohistochemical xenograft analysis. **a** A small but cellular SF188/V+ tumor in the *left side of the panel* contains dilated vessels (*arrows*) extending into host brain with few or no neoplastic cells on the *right*. A focus of hemorrhage is also present (*asterisk*). **b** A larger xenograft removed after 4 weeks of growth contains a number of massively dilated vessels (*asterisks*) with focal thrombosis. Vessels with lesser degrees of dilatation are also present (*arrow*). **c** In addition to vascular dilatation, proliferation of smaller vessels resulted in a dense network throughout most of the tumor (*arrows*). **d–f** Only weak VEGF immunoreactivity was present in SF188/V− cells, while SF188/V+ cells gave rise to xenografts with moderate to strong VEGF expression in and around vessels (*arrows*)

clinical studies have mostly been facilitated through the use of animal tumor models. However, there is currently no widely accepted glioma model that can closely mirror human GBM growth patterns. The 9L, F98, U87, U251, and many other cell lines are commonly used as glioma models, and to date have provided important information regarding glioma biology and therapy [7, 8]. However, it is known that each of these established glioma models has limitations. For example, 9L and F98 are not derived from human tumors; thus, they may have a different response, as compared to human gliomas. Although intratumoral hemorrhage is often encountered in human GBM, it is less common in most established tumor models, including U87 human tumor xenografts [10]. Further, as opposed to the highly heterogeneous, infiltrative pattern of the human disease, 9L, F98, U87, and U251 all have relatively homogenous, well-defined growth patterns with sharply demarcated tumor margins (Supplementary Fig. 1).

The transfection of VEGF cDNA into SF188/V− cells results in the SF188/V+ cell line that produces a high amount of VEGF [11]. Inoculating these cells in athymic rats produces tumor xenografts with prominent vascularity and hemorrhages, as reflected by particularly high blood flow and APT signals (Fig. 3; Table 1). The SF188/V+ tumor xenografts show scattered punctate hyperintense foci on the T_1-weighted images without contrast agents injected (Fig. 2). This important clinical feature likely reflects hemorrhagic changes, which are rarely observed in many established glioma models, such as 9L, F98, U87, and U251, as well as SF188/V−. The SF188/V+ glioma shows an extremely heterogeneous signal on the T_2-weighted images and a heterogeneous enhancement on the post-contrast T_1-weighted images (Figs. 1, 2). The presence of these key imaging and histopathology features of human GBM shows that SF188/V+ would be particularly beneficial for testing GBM response to anti-angiogenesis drugs.

Despite its advantages, the SF188/V+ glioma model has some limitations. First, in six athymic rats from our study, five inoculated with 5 million tumor cells and one inoculated with 3 million cells, the tumors started to shrink 4–5 weeks after formation and disappeared eventually (Supplementary Fig. 2). Despite the limitation, this model has morphological and vascularity characteristics that are similar to human GBM, and has the potential to be adapted to testing anti-angiogenesis agents. However, care should be taken when using this intracranial xenograft model, and the implanted tumor xenografts should be assessed using imaging modalities such as MRI, which would allow non-invasive, longitudinal, and real-time monitoring of tumor growth and shrinking.

While the heterogeneous nature of GBM is well mimicked on imaging, molecular heterogeneity is circumvented

by artificially overexpressing VEGF in all cells. This should be taken into account when interpreting and transferring the results obtained through this model to a clinical setting. A final limitation is the lack of significant infiltration of SF188/V+ glioma cells into the surrounding brain parenchyma. However, while further efforts towards developing a model completely mimicking the pathological, molecular, and radiographic characteristics of human GBM are still needed, the data presented here suggest that several key vascular features of these aggressive tumors are recapitulated by SF188/V+ cells, and these can be tracked using advanced imaging techniques.

Conclusions

In this study, we have investigated the imaging features and progression of SF188/V+ human glioma in a rat model. MRI demonstrated that the tumors had highly heterogeneous signals on the T_2-weighted images and a heterogeneous enhancement on the gadolinium-enhanced T_1-weighted images. Very large blood flow and APT signals were observed in the tumor, compared to contralateral brain tissue. These results clearly reflect the unique morphological and vascularity characteristics of the SF188/V+ glioma model that are potentially important for pre-clinical studies of anti-angiogenic therapy.

Acknowledgments The authors thank Dr. James M. Gallo (Temple University, Philadelphia, PA, USA; currently Mount Sinai School of Medicine, New York, NY, USA) for providing the glioma xenograft cell lines used in this study. The parental SF188/V− cell line was originally provided by the Brain Tumor Research Center, University of California, San Francisco, CA, USA. Dr. Jianguo Ma and Dr. James M. Gallo, et al. (Temple University, Philadelphia, PA, USA) made the SF188/V+ cell model. This study was supported in part by Grants from NIH (EB009112, EB009731, EB015032, and EB015555), by the American Physicians Fellowship (APF) for Medicine in Israel (Grossman), and by the Research Scholar Grants, #116293-RSG-08-119-01-CCE from the American Cancer Society (Tyler).

Disclosure The authors have no conflicting interests.

References

1. Wen PY, Kesari S (2008) Malignant gliomas in adults. N Engl J Med 359:492–507
2. Stupp R, Mason WP, van den Bent MJ, Weller M, Fisher B, Taphoorn MJB, Belanger K, Brandes AA, Marosi C, Bogdahn U, Curschmann J, Janzer RC, Ludwin SK, Gorlia T, Allgeier A, Lacombe D, Cairncross JG, Eisenhauer E, Mirimanoff RO (2005) Radiotherapy plus concomitant and adjuvant temozolomide for glioblastoma. N Engl J Med 352:987–996
3. Stupp R, Hegi ME, Mason WP, van den Bent MJ, Taphoorn MJ, Janzer RC, Ludwin SK, Allgeier A, Fisher B, Belanger K, Hau P, Brandes AA, Gijtenbeek J, Marosi C, Vecht CJ, Mokhtari K, Wesseling P, Villa S, Eisenhauer E, Gorlia T, Weller M, Lacombe D, Cairncross JG, Mirimanoff RO (2009) Effects of radiotherapy with concomitant and adjuvant temozolomide versus radiotherapy alone on survival in glioblastoma in a randomised phase III study: 5-year analysis of the EORTC-NCIC trial. Lancet Oncol 15:459–466
4. McGirt MJ, Than KD, Weingart JD, Chaichana KL, Attenello FJ, Olivi A, Laterra J, Kleinberg LR, Grossman SA, Brem H, Quinones-Hinojosa A (2009) Gliadel (BCNU) wafer plus concomitant temozolomide therapy after primary resection of glioblastoma multiforme. J Neurosurg 110:583–588
5. Shweiki D, Itin A, Soffer D, Keshet E (1992) Vascular endothelial growth factor induced by hypoxia may mediate hypoxia-initiated angiogenesis. Nature 359:843–845
6. Jain RK, Duda DG, Clark JW, Loeffler JS (2006) Lessons from phase III clinical trials on anti-VEGF therapy for cancer. Nat Clin Pract Oncol 3:24–40
7. Barth RF (1998) Rat brain tumor models in experimental neuro-oncology: the 9L, C6, T9, F98, RG2 (D74), RT-2 and CNS-1 gliomas. J Neuro-Oncol 36:91–102
8. Barth RF, Kaur B (2009) Rat brain tumor models in experimental neuro-oncology: the C6, 9L, T9, RG2, F98, BT4C, RT-2 and CNS-1 gliomas. J Neuro-Oncol 94:299–312
9. Goldbrunner RH, Wagner S, Roosen K, Tonn JC (2000) Model for assessment of angiogenesis in gliomas. J Neuro-Oncol 50: 53–62
10. Candolfi M, Curtin JF, Nichols WS, Muhammad AG, King GD, Pluhar GE, McNiel EA, Ohlfest JR, Freese AB, Moore PF, Lerner J, Lowenstein PR, Castro MG (2007) Intracranial glioblastoma models in preclinical neuro-oncology: neuropathological characterization and tumor progression. J Neuro-Oncol 85:133–148
11. Ma J, Zhou-Li F, Klein-Szanto A, Gallo JM (1998) Modulation of angiogenesis by human glioma xenograft models that differentially express vascular endothelial growth factor. Clin Exp Metastasis 16:559–568
12. Zhou Q, Guo P, Wang X, Nuthalapati S, Gallo JM (2007) Preclinical pharmacokinetic and pharmacodynamic evaluation of metronomic and conventional temozolomide dosing regimens. J Pharmacol Exp Ther 321:265–275
13. Zhou Q, Guo P, Gallo JM (2008) Impact of angiogenesis inhibition by sunitinib on tumor distribution of temozolomide. Clin Cancer Res 14:1540–1549
14. Verma R, Zacharaki EI, Ou Y, Cai H, Chawla S, Lee SK, Melhem ER, Wolf R, Davatzikos C (2008) Multiparametric tissue characterization of brain neoplasms and their recurrence using pattern classification of MR images. Acad Radiol 15:966–977
15. Chang SM, Nelson S, Vandenberg S, Cha S, Prados M, Butowski N, McDermott M, Parsa AT, Aghi M, Clarke J, Berger M (2009) Integration of preoperative anatomic and metabolic physiologic imaging of newly diagnosed glioma. J Neuro-Oncol 92:401–415
16. Wen PY, Macdonald DR, Reardon DA, Cloughesy TF, Sorensen AG, Galanis E, DeGroot J, Wick W, Gilbert MR, Lassman AB, Tsien C, Mikkelsen T, Wong ET, Chamberlain MC, Stupp R, Lamborn KR, Vogelbaum MA, van den Bent MJ, Chang SM (2010) Updated response assessment criteria for high-grade gliomas: response assessment in neuro-oncology working group. J Clin Oncol 28:1963–1972
17. Chenevert TL, McKeever PE, Ross BD (1997) Monitoring early response of experimental brain tumors to therapy using diffusion magnetic resonance imaging. Clin Cancer Res 3:1457–1466
18. Chenevert TL, Stegman LD, Taylor JMG, Roberson PL, Greenberg HS, Rehemtulla A, Ross BD (2000) Diffusion magnetic

resonance imaging: an early surrogate marker of therapeutic efficacy in brain tumors. J Nat Cancer Inst 92:2029–2035
19. Sinha S, Bastin ME, Whittle IR, Wardlaw JM (2002) Diffusion tensor MR imaging of high-grade cerebral gliomas. Am J Neuroradiol 23:520–527
20. Lu S, Ahn D, Johnson G, Cha S (2003) Peritumoral diffusion tensor imaging of high-grade gliomas and metastatic brain tumors. Am J Neuroradiol 24:937–941
21. Wolf RL, Wang JJ, Wang SM, Melhem ER, O'Rourke DM, Judy KD, Detre JA (2005) Grading of CNS neoplasms using continuous arterial spin labeled perfusion MR imaging at 3 tesla. J Magn Reson Imaging 22:475–482
22. Barrett T, Brechbiel M, Bernardo M, Choyke PL (2007) MRI of tumor angiogenesis. J Magn Reson Imaging 26:235–249
23. Alger JR, Frank JA, Bizzi A, Fulham MJ, Desouza BX, BDuhaney MO, Inscoe SW, Blake JL, van Zijl PCM, Moonen CTW, Dickiro G (1990) Metabolism of human gliomas—assessment with H-1 MR spectroscopy and F-18 fluorodeoxyglucose PET. Radiology 177:633–641
24. Nelson SJ, Graves E, Pirzkall A, Li X, Chan AA, Vigneron DB, McKnight TR (2002) In vivo molecular imaging for planning radiation therapy of gliomas: an application of ^{1}H MRSI. J Magn Reson Imaging 16:464–476
25. Ward KM, Aletras AH, Balaban RS (2000) A new class of contrast agents for MRI based on proton chemical exchange dependent saturation transfer (CEST). J Magn Reson 143:79–87
26. Zhou J, Payen J, Wilson DA, Traystman RJ, van Zijl PCM (2003) Using the amide proton signals of intracellular proteins and peptides to detect pH effects in MRI. Nat Med 9:1085–1090
27. Zhou J, Lal B, Wilson DA, Laterra J, van Zijl PCM (2003) Amide proton transfer (APT) contrast for imaging of brain tumors. Magn Reson Med 50:1120–1126
28. Zhou J, Tryggestad E, Wen Z, Lal B, Zhou T, Grossman R, Wang S, Yan K, Fu D-X, Ford E, Tyler B, Blakeley J, Laterra J, van Zijl PCM (2011) Differentiation between glioma and radiation necrosis using molecular magnetic resonance imaging of endogenous proteins and peptides. Nat Med 17:130–134
29. Wen Z, Hu S, Huang F, Wang X, Guo L, Quan X, Wang S, Zhou J (2010) MR imaging of high-grade brain tumors using endogenous protein and peptide-based contrast. NeuroImage 51:616–622
30. Jia GA, Abaza R, Williams JD, Zynger DL, Zhou JY, Shah ZK, Patel M, Sammet S, Wei L, Bahnson RR, Knopp MV (2011) Amide proton transfer MR imaging of prostate cancer: a preliminary study. J Magn Reson Imaging 33:647–654
31. Williams DS, Detre JA, Leigh JS, Koretsky AP (1992) Magnetic resonance imaging of perfusion using spin inversion of arterial water. Proc Natl Acad Sci USA 89:212–216
32. Gomori JM, Grossman RI, Goldberg HI, Zimmerman RA, Bilaniuk LT (1985) Intracranial hematomas—imaging by high-field MR. Radiology 157:87–93
33. Silva AC, Kim S-G, Garwood M (2000) Imaging blood flow in brain tumors using arterial spin labeling. Magn Reson Med 44: 169–173
34. Bernsen HJJA, van der Koger AJ (1999) Antiangiogenic therapy in brain tumor models. J Neuro-Oncol 45:247–255
35. Jain RK, Duda DG, Willett CG, Sahani DV, Zhu AX, Loeffler JS, Batchelor TT, Sorensen AG (2009) Biomarkers of response and resistance to antiangiogenic therapy. Nat Rev Clin Oncol 6:327–338